Research Article

Spectroscopic properties of red-emitting $Sr_{0.9}Na_{0.2}ZrO_3:Eu^{3+}$ phosphors with potential applications in lasers and LEDs

A. Nathan-Abutu [a,b], I. Ahemen [b], R.E. Kroon [c], A. Reyes-Rojas [a,*]

[a] *Materials Science Department. Centro de Investigacion' en Materiales Avanzados, S.C., Miguel de Cervantes 120, Complejo Industrial Chihuahua, 31109, Chihuahua, CHIH, Mexico*
[b] *Department of Physics, Federal University of Agriculture, P.M.B. 2373, Makurdi, Benue State, Nigeria*
[c] *Department of Physics, University of the Free State, PO Box 339, Bloemfontein, 9300, South Africa*

ABSTRACT

A range of $Sr_{0.9-y}Na_{0.2}ZrO_3: Eu^{3+}$ (SNEZ) nanocrystalline phosphors with high color purity and exceptional laser properties were synthesized using sol-gel technique. The samples were characterized for structural and spectroscopic properties using methods including X-ray diffraction (XRD), Raman spectroscopy, scanning electron microscopy (SEM), diffuse reflectance spectroscopy, and photoluminescence (PL) spectroscopy. Structural analysis revealed orthorhombic phase with average crystallite size 28-19 nm, decreasing with increasing Eu^{3+} concentration. A low phonon energy of 455–495 cm^{-1} and wide (expanding) band gaps (5.0–5.3 eV) were obtained for the SNEZ phosphors. Under the excitation of 300 nm, the SNEZ phosphor emits strong red light at 614 nm, attributed to the $^5D_0 \rightarrow {}^7F_2$ transition of the Eu^{3+} ion. Both XRD and Judd-Ofelt analysis revealed two sites for the Eu^{3+} ions. Additionally, the optimized SNEZ-7 phosphor achieves a PL internal quantum efficiency of 96 % under UV light at 300 nm excitation. Laser properties such as stimulated emission cross-section, gain bandwidth, branching ratio of the SNEZ phosphor is comparable to those of glasses, fluorides and other oxides for red light emitting laser applications. The CIE coordinate values of the synthesized red phosphor closely match those of commercially available red light-emitting phosphors, with a purity level of about 95 %. This suggests its suitability for various device applications, particularly in high-power white LEDs and lasers, as a red emitter.

1. Introduction

Ceramic materials with well-defined perovskite oxide structure having the molecular formula of ABO_3 have been used in various aspects of science and technology applications. Perovskite-type oxide phosphors are sufficiently conductive to release the charge stored on the surface of phosphor particles, which is a potential material for light-emitting diodes (LEDs).

The ideal perovskite (ABO_3) structure is a cubic structure with a space group Pm3 m (O_h). Cation A is coordinated by 12-oxygen ions, and cation B is coordinated by 6 oxygen ions. The structural BO_6 octahedra is connected by corner sharing in the A ion combination to fill the gaps between the octahedra. For the ZrO_6 octahedra, the radius of the void coincides with that of the 12-coordinated Sr^{2+}. The ionic radius of Sr^{2+} cations is smaller than the radius of the interstitial site for the ideal perovskite structure, thus the incorporation of the smaller-Sr cation at A tilts the ZrO_6 octahedra to fill the interstitial site and reach a 12-fold coordination (cuboctahedra). This is why $SrZrO_3$ belongs to the orthorhombic phase structure with *Pnma* space group. The luminescence-dynamics process of Eu^{3+} at $AZrO_3$ phosphors is greatly influenced by the tilting of the $[ZrO_6]$ octahedra creating oxygen vacancies [1–5].

Luminescent materials (phosphors) have garnered considerable attention for their ability to convert various excitation energies into visible radiation, leading to applications in lighting and displays technologies. Additionally, the low phonon energies in strontium and zirconium-based materials suggest they could enable longer-lasting lasers lighting application [6–12]. Luminescence is categorized based on the type of energy that triggers a material to emit light. This phenomenon involves light emission without heat and can be driven by various energy sources, including chemical reactions, electrical energy, radiation, or mechanical forces. In Plasma Display Panels (PDPs), luminescent materials are stimulated by the high-energy portion of the UV spectrum, whereas Field Emission Displays (FEDs) use low-voltage electrons to activate their phosphors [13,14]. The former's luminescence is

fundamental to this work and many other types of research, thanks to the search for new materials in the field of illumination light generation.

Rare earth (RE) ions have prominent sharp emission, hence doping them in oxide compounds have great potential applications in optoelectronics devices such as in display screens, light-emitting diodes (LEDs), imaging devices, sensors and photovoltaics, fiber-optic communications, lasers, scintillators, etc. [15–18]. With the discovery of blue emitting InGaN LEDs chips in 1997, more attention was drawn to WLEDs manufacturing by the combination of YAG: Ce^{3+} and blue InGaN LED chip [19,20]; but this combination produced a low color rendering index (CRI) and color correlated temperature (CCT) because of the insufficient emission within the red wavelength region. The introduction of red phosphors with UV/blue excitation is a way to compensate for this weakness [21,22]. Over these few decades, sulphide, oxynitrides or nitride were the basis of red phosphors [15], but showed some limitations such as, (i) the formation of a harmful toxic gas with an inadequate lifetime under UV excitation is associated with sulfide-based phosphors [21], (ii) nitride or oxynitride-based phosphor exhibit inefficient brightness, low color purity, and instability under UV excitation [23]. Due to the above drawbacks, the simplest strategy to generate white light is to stack red, green, and blue phosphors (tri-color) with UV/blue LED chip excitation [24]. Hence, it is essential in advancing the production of red-emitting phosphors for WLEDs with excitation under UV light.

Strontium zirconate ($SrZrO_3$) has been found in many applications such as crystalline hosts for phosphor materials, sensors, solid electrolytes, fuel cells, satellite broadcasting, and multilayer capacitors [25, 26]. There have been many reports on the luminescence of RE^{3+} ion-doped $SrZrO_3$ (an ABO_3 type) perovskite structures such as Eu^{3+}, Tb^{3+}, Ce^{3+}, Sm^{3+}, Dy^{3+}, Pr^{3+}, Gd^{3+} [27–32]. Among these different RE^{3+} ions, Eu^{3+} is a good luminescence activator in inorganic materials with sharp emission in the red spectral region due to its electronic transition in the $4f^6$ electron configuration. Just like other lanthanide metal ions, all six unpaired electrons contribute to its high electron spin [32]. Europium ions can act as optical centers and spectroscopic probes to gain insight into the effect of dopants on the lattice structure [33,34].

In this work, Eu^{3+} doped $Sr_{0.9-y}Na_{0.2}ZrO_3$ nanocrystalline phosphors was prepared in continuance with our previous research on the novel $Sr_{1-x}Na_{2x}ZrO_3$ perovskite nanocrystals [35] to improve the optical properties for luminescent applications. The large band gap of $Sr_{0.9}Na_{0.2}ZrO_3$ (5.0 eV) makes it transparent across the entire visible spectrum. This property can be functional to tune the color of $Sr_{0.9}Na_{0.2}ZrO_3$ through doping with rare-earth ions in order to extend its application. We also carried out spectroscopic studies using the Judd-Ofelt theory in order to determine its suitability for laser and LED applications. To the best of our knowledge, this is the first time Eu^{3+} is doped into $Sr_{0.9}Na_{0.2}ZrO_3$ nanocrystals.

2. Experimental details

2.1. Preparation of $Sr_{0.9-y}Na_{0.2}ZrO_3:Eu^{3+}$ phosphor materials

$Sr_{0.9-y}Na_{0.2}ZrO_3:Eu^{3+}$ (y = 0, 0.01, 0.03, 0.05, and 0.07; {further referred as y = 0 (SNEZ-0), y = 0.01 (SNEZ-1), y = 0.03 (SNEZ-3), y = 0.05 (SNEZ-5), y = 0.07 (SNEZ-7)}) phosphors were prepared via a sol-gel method. Analytical grades of strontium nitrate [$Sr(NO_3)_2$ (99.7 %)], Sodium nitrate [$NaNO_3$ (99.99 %)], Europium(III) nitrate [$Eu(NO_3)_3$ (99.9 %)], and Zirconium (IV) 2,4-pentanedionate, [$ZrC_{20}H_{28}O_8$ (99.72 %)] was used as received without further purification. At first, for the -undoped sample ($Sr_{0.9}Na_{0.2}ZrO_3$), the base solution for the synthesis was prepared in distilled water by adding 0.8579g of strontium nitrate, 0.0771g of Sodium nitrate, 2.1962g of Zirconium (IV) 2,4-pentanedionate, 1.8874g of citric acid and 0.8362g of ethylene glycol in 60 ml DI water under constant stirring for 5 h. We extend this by synthesizing $Sr_{0.9}Na_{0.2}ZrO_3$ samples doped with europium ions as doping elements from 1 to 7 % concentration according to the undoped procedure. The
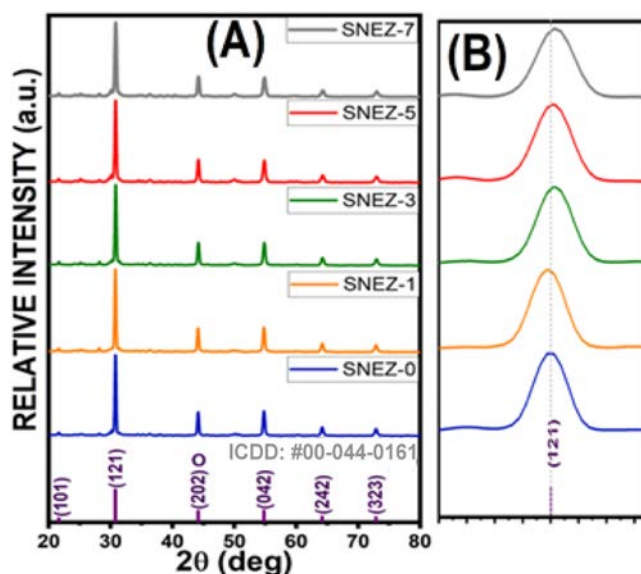

Fig. 1. (A) XRD patterns and (B) peaks shift of SNEZ phosphor.

stoichiometric ratio of precursor compounds was mixed in the 60 ml deionized (DI) water under vigorous stirring at ~70 °C for 5 h to form the xerogel. Then, the gel was transferred to the crucible and put into a furnace at 400 °C for 2 h for preheating. The SNEZ phosphor samples were obtained after annealing at 1050 °C for 4 h with 5 °C/min heating rate in a static air atmosphere, and then well crushed to fine powders for further characterization.

2.2. Characterization techniques

The crystalline phases of all synthesized samples were determined using an Empyrean diffractometer from PANalytical-Xpert powder X-ray diffractometer at 298 K using Cu Kα (λ = 1.5418 Å) radiation, divergence, and reception slits of 1° in continuous scan mode, 40 kV voltage, 30 mA current, 0.01°/s scan speed and 2θ angular range from 20° to 80°. Diffraction patterns were determined using crystallographic records from the Joint Committee on Powder Diffraction Standards - International Center for Diffraction Data (JCPDS-ICDD) database. An estimation of the average crystallite sizes of the analyzed samples was performed using the Scherrer equation. Scanning electron microscopy (SEM) and energy dispersive X-ray spectra (EDS) were taken on a Hitachi SU3500 SEM. Fourier transform infrared (FTIR) spectroscopy was obtained on an AIM-9000 FTIR Spectrometer in the wave number region 400 cm^{-1} to 4000 cm^{-1}. Raman spectra were recorded in the 100–1100 cm^{-1} range using an XploRA INV-Horiba inverted Raman microscope using a 532 nm laser with 50 mW power. The UV–vis diffuse reflectance spectra were obtained at room temperature using DRS, Shimadzu UV-1280 UV–vis spectrophotometer. Photoluminescence (PL) emission spectra in the UV-NIR range (350–750 nm) were recorded using a photomultiplier tube (PMT) detector at room temperature while the sample was excited by a He–Cd laser with a wavelength of 325 nm for the luminescent analysis.

3. Results and discussions

3.1. Powder X-ray analysis and structure of SNEZ phosphor

Fig. 1(A) shows the powder X-ray diffraction (PXRD) profiles of the Europium ions incorporated SNZ nanoparticles. According to our previous results concerning the crystal structure refinement by the Rietveld method, the solid solution crystallizes in an orthorhombic structure [35]. As depicted in the figure, the diffraction profile closely matches the

Table 1
Estimated mean crystallite size, optical bandgap, for SNEZ phosphors.

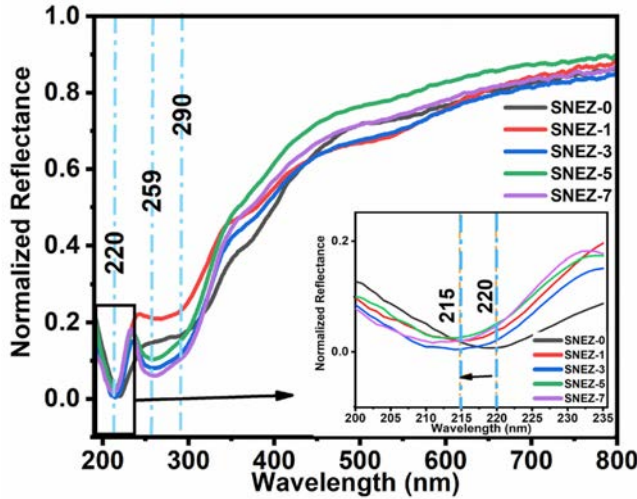| Sample Identity	Eu^{3+} Conc. (mol %)	Crystallite size (nm)	Energy Band gap (eV)
SNEZ-0	0	28	5.00
SNEZ-1	1	26	5.21
SNEZ-3	3	25	5.26
SNEZ-5	5	22	5.29
SNEZ-7	7	19	5.33

Fig. 2. Normalized Diffuse Reflectance spectra of SNEZ phosphors annealed at 1050 °C for 4 h.

perovskite orthorhombic structure of SrZrO$_3$ (ICDD card No. 00-044-0161) with the *Pnma* space group. No significant phase change was observed in the doped samples, indicating complete doping of the Eu^{3+} ions into the host lattice. Furthermore, the addition of impurity ions (Eu^{3+}) to the matrix does not induce alterations in the crystal structure. From Fig. 1(B), it is evident that the XRD peaks of the doped samples are shifted towards higher diffraction angles, consistent with the reduction of the unit cell volume resulting from the incorporation of a larger ion in place of a smaller one. Since the orthorhombic perovskite structure is a distorted form of an ideal ABO$_3$ cubic structure, the co-ordination of O^{2-} for the A sites is lowered from twelve to eight. Thus, for the Sr$_{0.9-y}$Na$_{0.2}$ZrO$_3$ we would consider eight coordination number (CN) for the cuboctahedron consisting of Na$^+$, Sr^{2+} and Eu^{3+} with ionic radii of 1.18 Å, 1.26 Å and 1.07 Å, respectively, and in the octahedron, CN = 6, Zr^{4+} = 0.72 Å and Eu^{3+} = 0.95 Å [36,37]. Therefore, the only pair substitution (dopant to host ion substitution) responsible for the displacement of the (hkl) diffraction peaks towards larger angles will be the incorporation of higher percentage of Eu^{3+} (larger ion) at the smaller Zr^{4+} sites in the ZrO$_6$ octahedra. The slight difference in valence electron between Eu^{3+} and Zr^{4+} also favors this substitution with some form of charge compensation. The compensating ion may not be identical at all substitution sites, which means they may not occupy exactly the same position with respect to the axes of the crystal field. Because of the larger difference of ionic radii between Eu^{3+} and Zr^{4+} than between Eu^{3+} and Na$^+$/Sr^{2+} cations, the incorporation of Eu^{3+} at the site of Zr^{4+} would induce larger distortion of the crystal lattice. Thus, from the forgoing, there are two sites occupied by the Eu^{3+} ions; the less distorted (more symmetric) Na$^+$/Sr^{2+} sites and more distorted (less symmetric) Zr^{4+} sites.

The crystallite sizes of all samples were determined using the Scherrer's equation, and their values are provided in Table 1. The average observed crystallite size decreases monotonically as the
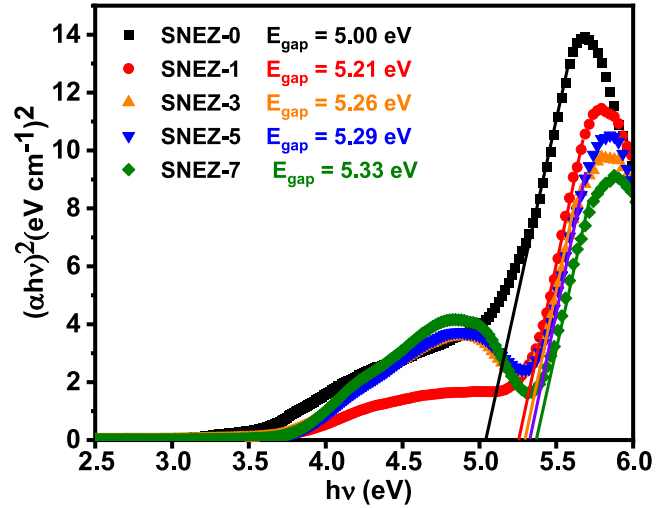

Fig. 3. Optical bandgap energy of SNEZ phosphors.

concentration of dopant ions increases, from 28 nm to 19 nm. The presence of dopant atoms impedes the growth of crystallite size, leading to a smaller size overall. This decrease in crystallite size stems from lattice distortion induced by the variance in radius between the dopant and the original element it replaces. In perovskites with ABO$_3$, hetero-valent dopants can be either donor or acceptor types. In the case of donor dopants, they have a surplus of positive charge relative to the substituted A ion, which is balanced by the creation of cation vacancies. These vacancies interact with oxygen vacancies and limit their mobility. As oxygen vacancies play a crucial role in structural mobility, the result is a decrease in crystalline size.

3.2. Band gap and optical properties of SNEZ phosphor

The UV–visible diffuse reflectance spectra recorded (190–800 nm) of Eu^{3+} doped Sr$_{0.9-y}$Na$_{0.2}$ZrO$_3$ samples were obtained and illustrated in Fig. 2. There was a slight difference in the absorption band of undoped and Eu^{3+} doped samples. The undoped sample displayed two absorption bands at 220 and 290 nm. For Eu^{3+} doped samples, these bands shift to lower absorption bands (blueshift) at 215 nm (see Fig. 2 insert) and 259 nm. The absorption bands at 215, 220 and 290 nm are ascribed to the host absorption band involving electron transfer between Zr^{4+} and O^{2-} and intrinsic defect states [38,39].

The Kubelka-Munk (K-M) model, adjusted with the Tauc-Wood relationship, was employed to determine the energy-appropriate optical bandgap properties of the synthesized perovskite, as demonstrated in both our prior studies and other published research [40–42]. The direct optical-energy band gap (E_g) was obtained directly from the plot of $[h\nu \, F(R)]^2$ vs. $h\nu$ from $[F(R)h\nu]^2 = K(h\nu - E_g)$ expression [43,44]. The energy band gap of the phosphors $h\nu$ was determined from the inter-section point on the ordinate, as illustrated in Fig. 3. SrNaZrO$_3$ phos-phors doped with europium exhibit slightly larger band gaps (E_g) of $\approx 5.21, 5.26, 5.29$ and 5.33 eV, respectively. The host material SNZ has a band gap of 5.00 eV (refer to Table 1). The optical bandgap of SNEZ phosphors, ranging from 5.00 to 5.33 eV, falls within the intrinsic band gap of SrZrO$_3$ (4.00–5.60 eV), which is characteristic of large-gap semiconductors. This range has been noted by other researchers for its potential in efficient visible-light applications [45–47]. The observed variations in the optical bands suggest two primary factors: (I) the emergence of defects in the crystal structure and (II) an augmentation of charge carriers in the conduction band resulting from the Eu^{3+} doping process. This augmentation indicates a shift in the Fermi level, a phe-nomenon associated with the 'Moss–Burstein shift'. Following the introduction of europium, the energy bandgap of the phosphor
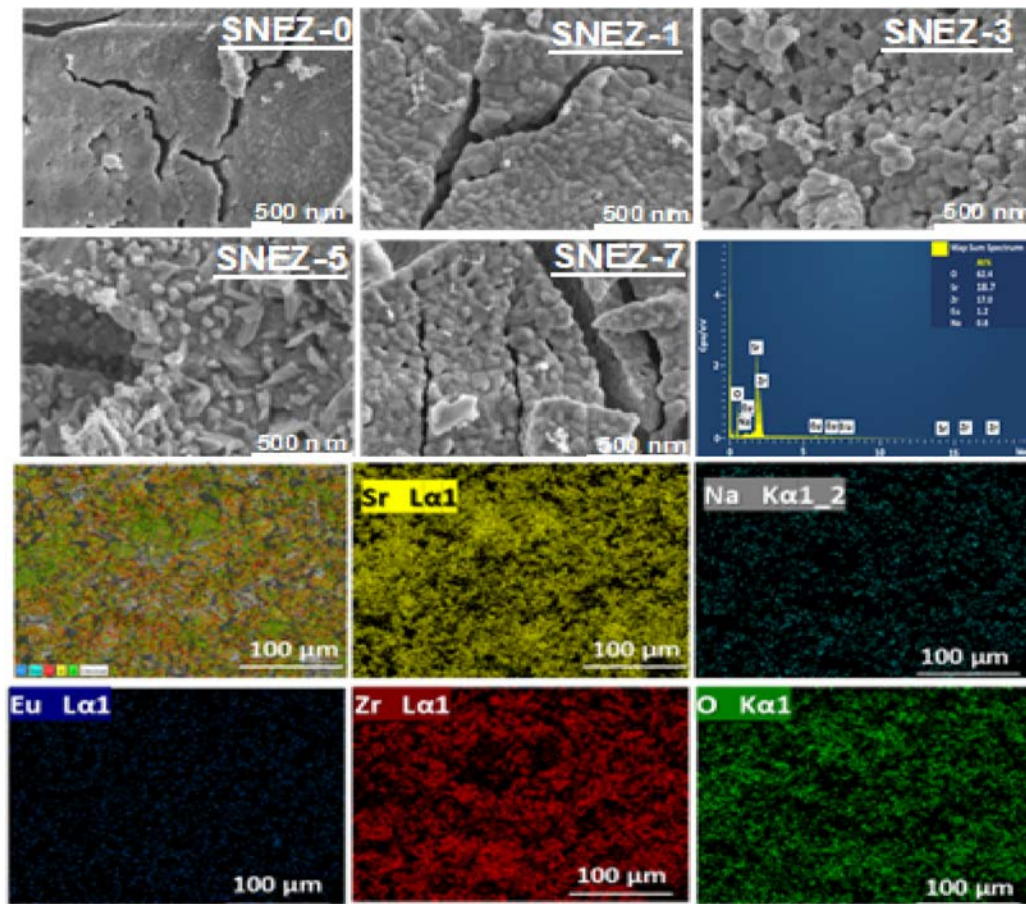
Fig. 4. SEM images for the SNEZ samples as well as EDS and mapping images of SNEZ-7.

Table 2
Quantitative EDS analysis of SNEZ nanophosphors.

Element	At. %					Energies (keV)
	SNEZ-0	SNEZ-1	SNEZ-3	SNEZ-5	SNEZ-7	
Oxygen (O)	57.3	56.7	62.8	62.0	62.3	$K\alpha_1$ (0.523)
Zirconium (Zr)	25.4	21.7	17.5	19.3	17.0	$L\alpha_1$ (2.042)
Strontium (Sr)	16.1	20.4	18.5	16.8	18.7	$L\alpha_1$ (1.806)
Sodium (Na)	1.2	1.0	0.6	0.9	0.8	$K\alpha_{1\_2}$ (1.040)
Europium (Eu)	–	0.2	0.6	1.0	1.2	$L\alpha_1$ (5.845)

undergoes a gradual increase. The incorporation of Eu^{3+} ions into the lattice introduces intermediate energy levels near the conduction and valence band edges, leading to a widening of the band gap. The modified optical bandgap data indicate that the fabricated phosphor material can be intentionally tuned, allowing for deliberate adjustments in its optical and optoelectronic properties.

3.3. Scanning electron microscopy analysis of SNEZ phosphor

The morphology and particle size of SNEZ phosphor were examined via SEM and Energy-dispersive spectroscopy (EDS). EDS was employed to determine the elemental composition of the nanophosphor materials in atomic percent (at. %). Fig. 4 presents SEM images of the SNEZ
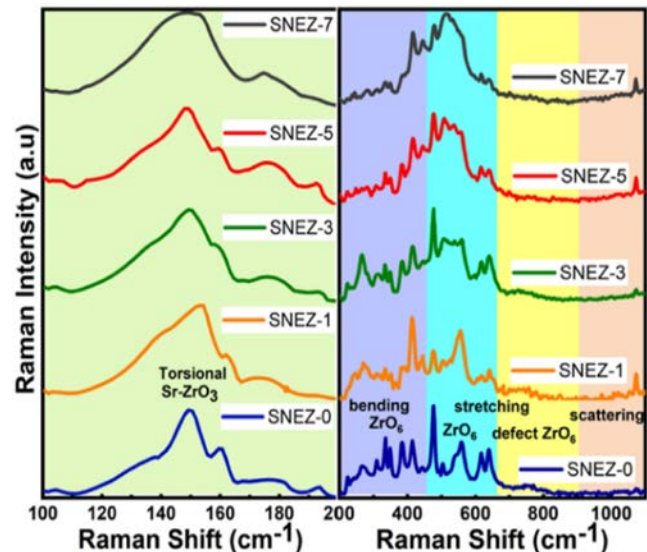

Fig. 5: (A). Wide scan Raman spectra for SNZ-0 to SNEZ-7 samples.

samples, revealing densely packed, irregular, and agglomerated particles with sizes ranging from 148 nm to 350 nm. The observed morphologies are attributed to the substantial release of gas during the combustion reaction at elevated temperatures [35,48]. With increasing concentrations of europium, there's a noticeable shift in the morphology
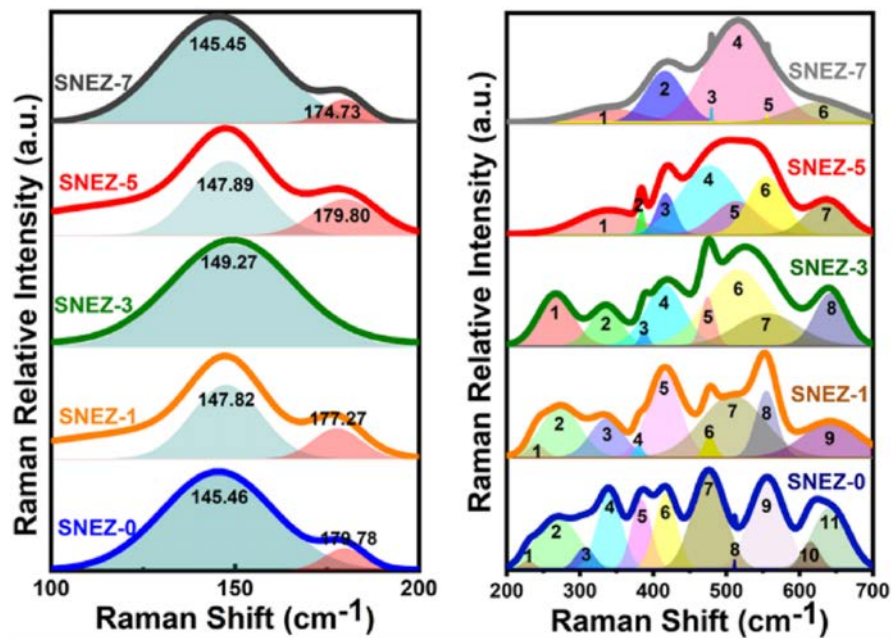
Fig. 5: (B). Raman vibration mode and deconvolution for SNEZ-0 to SNEZ-7 samples.

from tightly packed agglomerates to a more porous structure, indicating the growing influence of the dopant on the surface characteristics. Analysis of Energy-dispersive spectroscopy (EDS) spectra for SNEZ at various concentrations indicates the presence of Sr, Na, O, Zr, and Eu elements in the sample, with no detection of other impurity elements. Quantitative EDS analysis of the nanophosphor materials, as detailed in Table 2, reveals that the concentrations of constituent elements closely align with theoretical stoichiometry. The even distribution of elements within the sample is affirmed by the mapping images of SNEZ-7.

3.4. Raman spectra studies of SNEZ phosphor

Raman spectroscopy, known for its vibrational sensitivity, stands out as a precise and effective method for identifying the local environment of cations. Consequently, it is anticipated to be instrumental in determining the localization of europium ions within the strontium sodium zirconate lattice as the SNZ nonstoichiometric is varied. Illustrated in Fig. 5(a) are the Raman spectra at ambient conditions for SNEZ-0 to SNEZ-7, spanning the frequency range of 90–1200 cm^{-1}. This figure serves as an exemplar of a typical spectrum for the europium-doped strontium sodium zirconate material, as explored in this study. The presence of double vibration modes within the range of 145–179 cm^{-1}, corresponding to the torsional vibration of $SrZrO_3$, across all spectra, serves as confirmation of the orthorhombic *Pnma* symmetry exhibited by the samples. These vibrational modes align with those reported by various researchers for the orthorhombic *Pnma* space group of $SrZrO_3$ [35,49–52].

To delve deeper into the Raman vibration modes, Gaussian deconvolution was applied to each spectrum depicted in Fig. 5(b) which illustrates the torsional vibration with defined peak frequencies of 145–149 cm^{-1} (B_{2g} symmetry) and 174–179 cm^{-1} (A_g symmetry). The second vibration motion, known as 'stretching', is primarily induced by changes in the Zr–OI bond length, while the third vibration, referred to as 'bending', results from alterations in the OII–Zr–OI bond angle [51–53].

The partial substitution of the B site by another element, along with oxygen deficiency, induces a slight displacement of the zirconium ion, leading to distortion and tilt angles of the ZrO_6 octahedron. The shift in the positions of the lattice vibration peaks in ABO_3 perovskite is

Table 3

Raman Peaks Positions (cm^{-1}), their assignment and Phonon energy for SNEZ samples from Fig. 5(B).

Peak Index	SNEZ-0	SNEZ-1	SNEZ-3 (Raman Symmetry)	SNEZ-5	SNEZ-7
1	229.1 (A_g)	239.2 (A_g)	266.9 (A_g)	339.3 (B_{3g})	338.1 (B_{3g})
2	269.4 (A_g)	274.4 (A_g)	335.6 (B_{3g})	383.9 (B_{1g})	381.4 (B_{1g})
3	306.9 (B_{3g})	335.6 (B_{3g})	385.1 (B_{1g})	417.2 (A_g)	415.9 (A_g)
4	340.6 (B_{1g})	378.9 (B_{1g})	415.9 (A_g)	477.2 (B_{2g})	479.6 (B_{2g})
5	383.9 (B_{2g})	414.7 (A_g)	475.9 (B_{2g})	513.6 (B_{2g})	555.9 (B_{3g} or B_{1g})
6	417.2 (A_g)	477.2 (B_{2g})	514.9 (B_{2g})	554.8 B_{3g} or B_{1g}	629.3 (B_{3g})
7	475.9 (B_{2g})	510.0 (B_{2g})	557.2 (B_{3g} or B_{1g})	637.5 (B_{3g})	
8	511.2 (B_{2g})	554.8 (B_{3g} or B_{1g})	642.7 (B_{3g})		
9	555.9 (B_{3g} or B_{1g})	651.6 (B_{3g})			
10	614.8 (A_g)				
11	642.3 (B_{3g})				
Average Phonon Energy (cm^{-1})	455	456	470	492	495

fundamentally a result of defects. The presence of Raman modes in the 600 - 650 cm^{-1} spectral region, indicative of the defective oxygen sublattice region of stretching vibrations, is observed for all sample components [54–56]. The deconvolution of the second and third vibrations (200–700 cm^{-1}) is presented in Fig. 5(B). The peak positions of all SNEZ modes align with those obtained by other researchers for
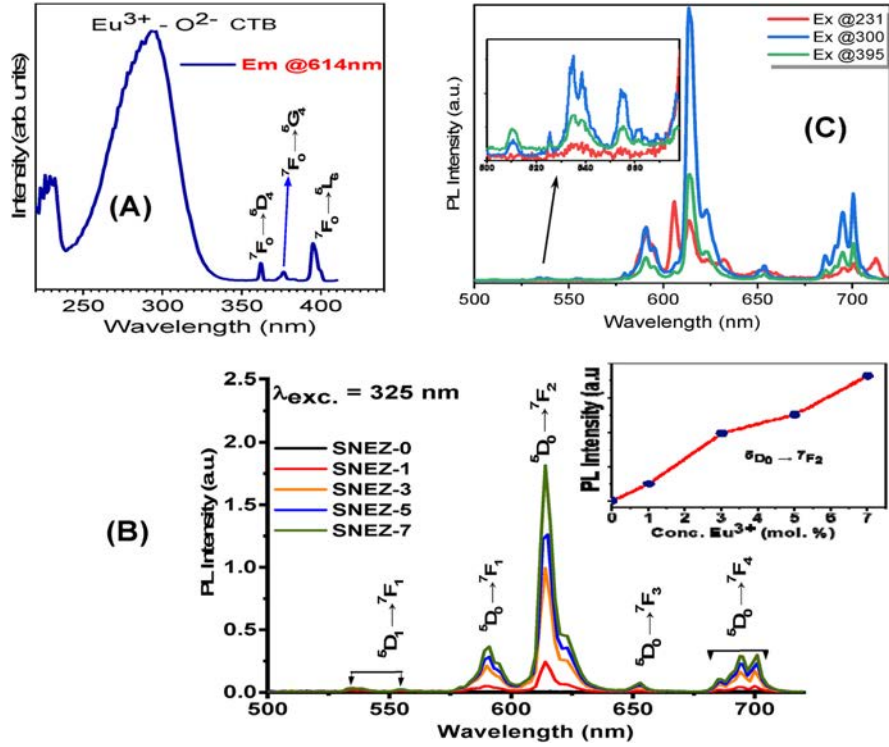
Fig. 6. (A) Representative excitation spectrum (emission at 614 nm), (B) PL emission spectra of Eu^{3+} doped SNZ nanophosphor, (insert) emission intensity with Eu^{3+} concentration, (C) Room Temperature emission of SNEZ-7 at different Excitations.

different zirconates [35,51,52,54]. Table 3 summarizes the positions, relative intensities, and phonon energies of the observed Raman peaks for the perovskite-type SNEZ based compositions.

The irreducible representations Γ of the SrZrO$_3$ crystal $\Gamma^{vib.}_{SrZrO3}$ with a *Pnma* space group is given as:

$$\Gamma^{vib.}_{SrZrO3} = 7A_g + 5B_{1g} + 7B_{2g} + 5B_{3g} + 8A_u + 10B_{1u} + 8B_{2u} + 10B_{3u} \quad (1)$$

Only 24 fundamental lattice vibrations having Raman polarizability tensors are Raman active, these are:

$$7A_g + 5B_{1g} + 7B_{2g} + 5B_{3g} \quad (2)$$

For SNEZ-0, the Raman spectra revealed 13 bands within the 100-700 cm^{-1} range. This relatively high number of bands can be attributed to the low polarizabilities of certain modes and small distortions in the SNZ crystal, which can lower the spectral resolution. The number of bands gradually decreases for subsequent compositions: SNEZ-1 (11 bands), SNEZ-3 (10 bands), SNEZ-5 (9 bands), and SNEZ-7 (8 bands). The observation suggests that as the concentration of europium in the sample increases, the number of Raman symmetries decreases (refer to Table 3). The decline in Raman symmetries as dopant concentration rises arises from lattice distortions and disorder prompted by dopant ions, which modify vibrational modes and introduce localized ones within the crystal lattice. Furthermore, the deviation from the original symmetry is influenced by charge transfer effects occurring between dopant ions and the lattice.

The phonon energy characterizes the resonant energy of lattice vibrations within a material. The concept suggests that materials with low phonon energy are deemed more suitable hosts for certain rare earth (RE) species. This preference arises because the relaxation of the excited REs may occur through the transfer of multiple phonons, leading to a less probable relaxation process. An effective phonon energy (E_{ph}) to review the radiationless transition rate of the SNEZ nanophosphor was determined from the expression [57]:

$$E_{ph} = \frac{\sum_i E_i w_i A_i}{\sum_i w_i A_i} \quad (3)$$

where E_i, w_i and A_i are the position, FWHM, and relative intensity of each Gaussian sub-band fitting, respectively. The calculated phonon energies (E_{ph}) for the SNEZ-0 to SNEZ-7 nanophosphors fall within the range of 455 cm^{-1} to 495 cm^{-1}. The presence of low phonon energy in these materials reduces the probability of non-radiative multiphonon relaxation of activated ions within the vibrational bands of the host lattice. Consequently, the low phonon energies observed in SNEZ materials hold the promise of higher quantum efficiency in photoluminescence and longer lifetimes of the excited state [35,52].

3.5. Luminescence analysis of SNEZ phosphor

The room temperature photoluminescence excitation spectrum for the 614 nm emission is depicted in Fig. 6(A), showcasing peaks at 231 (200–240), 300 (240–380), 362, 377, and 395 nm. The indirect excitation bands observed in the range 200–240 nm (peak maximum at 231 nm) and 240–380 (peak maximum at 300 nm) are attributed to the O^{2-} - Zr^{4+} electron transfer of the host absorption band and O^{2-} - Eu^{3+} charge transfer band (CTB), respectively [58,59]. On the other hand, the excitation lines at 362, 377 and 395 nm corresponding to the $^7F_2 \rightarrow {}^5D_4$, $^7F_2 \rightarrow {}^5L_7$, and $^7F_2 \rightarrow {}^5L_6$ transitions, respectively of Eu^{3+} ion are direct excitation bands. Photoluminescence (PL) emission spectra of SNEZ measured at room temperature are illustrated in Fig. 6(B). The emission spectrum recorded with under 325 nm wavelength excitations show exclusively the intraconfigurational transitions of Eu^{3+} ion; $^5D_1 \rightarrow {}^7F_1$ (523/545 nm), $^5D_0 \rightarrow {}^7F_1$ (592 nm), $^5D_0 \rightarrow {}^7F_2$ (614/625 nm), $^5D_0 \rightarrow {}^7F_3$ (652 nm), and $^5D_0 \rightarrow {}^7F_4$ (700 nm). The PL emission spectra exhibit the same profile and peak position for all sample, but the intensities at $^5D_0 \rightarrow {}^7F_2$ transition remarkably increases with increasing concentration of Eu^{3+} ions (see Fig. 6(B) insert). The continuous rising trend of the $^5D_0 \rightarrow$
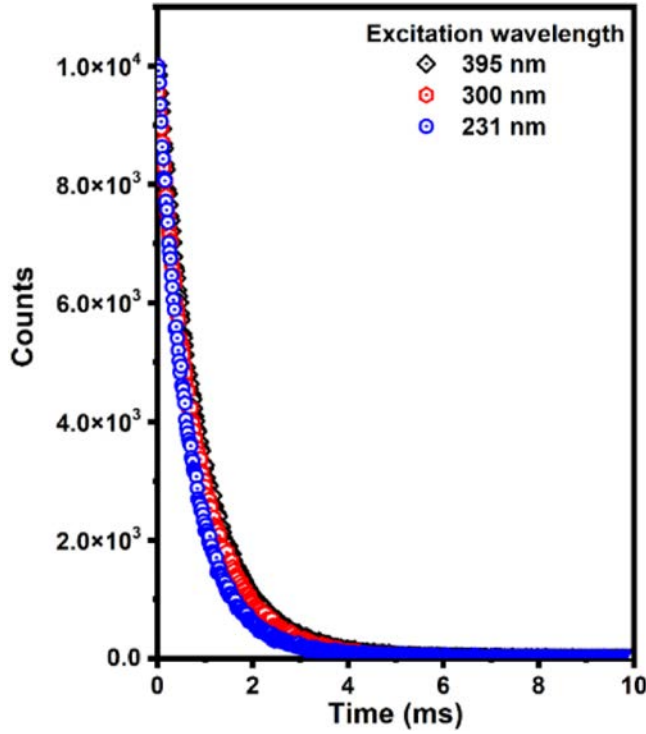
Fig. 7. Decay profiles SNZE-7 at different excitation wavelengths.

$^7F_2$ transition intensity is synonymous to increasing lattice distortion around the Eu^{3+} ions as confirmed by the Raman result. For the purpose of more critical analysis, going forward, we would only be considering the SNEZ-7 sample giving that within the limit of Eu^{3+} concentration range taken in this work, it produced the strongest emission intensity.

Room temperature PL spectra for the SNEZ-7 sample under 231, 300, and 395 nm excitation wavelengths are presented in Fig. 6(C). In both indirect (231/300 nm) and direct excitation (395 nm), the spectra present emission lines as listed for the 325 nm excitation wavelength, except that there is an addition of emission line at 579.5 nm corresponding to the $^5D_0 \rightarrow {}^7F_0$ transition and also the difference in their relative intensities. The dominance of the $^5D_0 \rightarrow {}^7F_2$ transition over the $^5D_0 \rightarrow {}^7F_1$ transition is an indication that the environment surrounding Eu^{3+} in the samples is non-centrosymmetric with no center of inversion symmetry [60–64]. The emission intensity under indirect excitations (at 300 nm) is strongest, suggesting that the emission mechanism is dominated by energy transfer from host to Eu^{3+}. It can also be noted from Fig. 6(C) that the transitions split into component lines (stark splitting). In particular, looking at Fig. 6(C) under host excitation band (231 nm), only one line for J = 0 → J = 0 (579.5 nm), three lines for J = 0 → J = 1 (591, 594 & 596 nm) and four lines for J = 0 → J = 2 (606, 614, 624 & 632 nm) transitions. On the other hand, the PL spectra under CTB (300 nm) and direct excitation (395 nm) show the following Stark components; one line for J = 0 → J = 0 (579.5 nm), two lines for J = 0 → J = 1 (591 & 595 nm) and two lines for J = 0 → J = 2 (614 & 623 nm) transitions. The difference in the number of Stark splitting components of 614 nm peak shows there are two sites of slightly different symmetries/crystal field strengths for Eu^{3+} ions in the host matrix. This is in agreement with the XRD result which confirm the existence of two sites. Since the $^5D_0 \rightarrow {}^7F_2$ transition is dominant for the two categories of excitation wavelengths, it therefore suggests that the symmetries of the two sites are similar but vary in their degree of asymmetry. The degree of distortion is more when Eu^{3+} substituted Zr^{4+} because of the large dissimilarity in their ionic radii as elucidated in the XRD analysis. This size effect together with oxygen vacancies generated for charge compensation leads to a larger stark splitting of transition levels as

observed for the same sample excited by 231 nm source than at 300/395 nm (Fig. 6(C)). It should be noted that both the Sr^{2+} site in cuboctahedron and Zr^{4+} site in the octahedron of an ideal perovskite share the same O_h point group symmetry [65]. However, the $^5D_0 \rightarrow {}^7F_0$ transition is not allowed for the O_h point group and the $^5D_0 \rightarrow {}^7F_2$ transition is expected to be single unsplit [66]. Thus, we infer that the symmetry sites under both set of excitations are lower than the O_h point group symmetry. Moreover, the $^5D_0 \rightarrow {}^7F_0$ transition is allowed in only 10 site symmetries; C_s, C_1, C_2, C_3, C_4, C_6, C_{2v}, C_{3v}, C_{4v}, and C_{6v} [67] which lack inversion symmetry, Therefore, for the orthorhombic structure, the stark component matches the C_{2v} point group symmetry around the Eu^{3+} ions for the 231 nm excitation wavelength. But, under the 300/395 nm excitation wavelength, the stark components did not match any point group symmetry of the orthorhombic class in the selection rule table given in Ref. [68], indicating that the site symmetry of Eu in SNZE-7 nanocrystals is much lower and is likely C_{4v} symmetry. Thus, we can conclude that both sets of excitation wavelengths excites Eu^{3+} ions at Zr^{4+} sites but in two different environments; one at a short range close to zirconium vacancies with C_{2v} symmetry and the other at a long range to the zirconium vacancies with C_{4v} symmetry in the SNZE-7 nanocrystals. A similar observation was reported by Gupta et al. [66,69].

The decay profile for the 614 nm emission under direct and indirect excitations are presented in Fig. 7. Under both excitations, a biexponential decay fitting gave the best results. Biexponential fit reveals the presence of more than one environment for the Europium ions as previously noted. The collected data were fitted to a double exponential function, facilitating the computation of the average luminescent lifetime through the following equation:

$$I(t) = \sum_{i=1,2,3} I_i \exp\left(-t / \tau_i\right) \tag{4}$$

In this expression, $I(t)$ represents the luminescence intensity, t denotes the time elapsed since excitation, and τ_i refers to the decay time of the ith component, accompanied by an intensity of I_i. The average lifetime was determined utilizing the following expression:

$$\tau_i = \frac{\sum\limits_{i=1,2,3} I_i \tau_i^2}{\sum\limits_{i=1,2,3} I_i \tau_i} \tag{5}$$

The calculated average decay lifetimes (τ_{ave}) are 0.86 ms, 0.89 ms, and 0.93 ms for excitation wavelengths of 231, 300, and 395 nm, respectively. The increasing trend of average decay lifetime with increasing excitation wavelength can be attributed to the increased amount of radiative energy reaching the Europium ions.

3.5.1. Judd-Ofelt parameters and internal quantum efficiency determination

Spectroscopic properties of SNEZ-7 nanophosphors such as spontaneous radiative emission rate A_{rad}, phenomenological intensity parameters Ω_J and simulated emission cross-section δ_k were determined from Judd-Ofelt (JO) theory in order to assess the applicability of the phosphors for red light emitting LEDs and lasers [70]. These spectroscopic properties can be obtained from the emission spectra in Fig. 6(B). The choice of SNEZ-7 is deliberate as it produced the strongest emission of all the spectra measured. Furthermore, we determine the parameters using the emissions spectra under three excitation wavelengths; 231, 300 nm and 395 nm. This was done in order to find which excitation wavelength produced the best properties.

The JO intensity parameters were obtained from the integrated intensities of $^5D_0 \rightarrow {}^7F_1$ $(i.e., \int I_{0-1}(\bar{v})d\bar{v})$ and $^5D_0 \rightarrow {}^7F_{J=2,4}$ $(i.e., \int I_{0-J}(\bar{v})d\bar{v})$ transitions by employing the expression [54];

$$\Omega_2 = \frac{D_{MD}\bar{v}_1^3}{e^2\bar{v}_J^3 U^J} \frac{9n^3}{(n^2+2)^2} \frac{\int I_{0-J}(\bar{v})d\bar{v}}{\int I_{0-1}(\bar{v})d\bar{v}} \tag{6}$$

Table 4
Intensity parameters, radiative parameters, experimental lifetime, quantum efficiency and asymmetry ratios of SNEZ-7 nanophosphors at different excitation wavelengths.

Excitation Wavelength (nm)	Ω_2 (10^{20} cm^2)	Ω_4 (10^{20} cm^2)	A_{rad} (s)	A_{nr} (s)	τ_{rad} (ms)	τ_{exp} (ms)	η %	R_0
231	3.67	3.67	420	747	2.38	0.86	36	1.3
300	11.41	6.64	1086	45	0.92	0.89	96	7.9
395	4.58	2.80	440	633	2.27	0.93	41	7.1

where $D_{MD} = 9.6 \times 10^{-42} esu^2 cm^2$ is the magnetic dipole line strength of the $^5D_0 \rightarrow {}^7F_1$ transition, which is taken as a reference for all transitions emanating from the $^5D_0$ level, $\bar{v}$ is the energy barycenter in cm^{-1} for a given transition, n is effective refractive index and $U^J = \lfloor \langle J \| U^J \| J' \rangle \rfloor^2$ is the reduced matrix element of electric dipole transition emanating from the state J' ($^5D_0$) to state J ($^5D_0 \rightarrow {}^7F_{J=2,4}$). The values of $U^2 = 0.00324$ and $U^4 = 0.00229$ are taken from these references [72,73].

The spontaneous radiative probability rate, A_{rad} is given by;

$$A_{rad} = \sum_{J=2,4} A_{0-J} + A_{0-1} \tag{7}$$

where A_{0-J} is the transition rate due to electric dipole transitions ($^5D_0 \rightarrow {}^7F_{J=2,4}$) and A_{0-1} is the transition rate due to the magnetic dipole transition ($^5D_0 \rightarrow {}^7F_1$) [51]. The values of A_{0-1} and A_{0-J} were calculated using equations (8)–(11) [71,74,75];

$$A_{0-J} = \frac{64\pi^4}{3h} \frac{\bar{v}_J^3 n(n^2+2)^2}{9} D_{ED}^J = 8.034 \times 10^9 \bar{v}_J^3 n(n^2+2)^2 \Omega_J U^J \tag{8}$$

$$D_{ED}^J = e^2 \Omega_J U^J \tag{9}$$

$$A_{0-1} = \frac{64\pi^4 \bar{v}_1^3 n^3}{3h} D_{MD} = 3.009 \times 10^{-12} \bar{v}_1^3 n^3 \tag{10}$$

$$D_{MD} = \frac{e^2 \hbar^2}{4m_e^2 c^2} \left| \langle 4f^N SLJ \| L + g_s S \| 4S'L'J' \rangle \right|^2 \tag{11}$$

where $n = 1.97$, $h = 6.63 \times 10^{-27}$ ergs.s, $e = 4.803 \times 10^{-10}$ esu, $m_e = 9.10904 \times 10^{-28} g$ and D_{ED}^J are the effective refractive index, Planck's constant, electronic charge, electron mass, and electric dipole line strength corresponding to given $^5D_0 \rightarrow {}^7F_{J=2,4}$ transitions. The Lorentz local field correction factor is $n(n^2+2)^2/9$ and the bracketed term in equation (11) is the reduced matrix element of the magnetic dipole transition. The radiative life time, τ_{rad} was obtained from equation (7);

$$\tau_{rad} = \frac{1}{A_{rad}} \tag{12}$$

The value of effective refractive index, n was calculated for SNEZ nanophosphors using the average energy bandgap value (E_g) for the corresponding doped sample by applying the simplified Dimitrov and Sakka relation [76,77] given as;

$$n = \left[\left(\frac{180}{E_g} \right)^{1/2} - 2 \right]^{1/2} \tag{13}$$

Using equations (6)–(13), the values of JO parameters were calculated and presented in Table 4 for the SNEZ-7 sample excited at 231, 300 and 395 nm wavelengths. The calculated values of intensity parameters, Ω_2 and Ω_4 are such that $\Omega_2 > \Omega_4$ for all excitation wavelengths. The Ω_4 has a long-range effect and explains the rigidity of the host matrix while Ω_2 has a short-range effect and indicate the covalence of Europium with the local field as well as the distortion around the dopant ion. The larger values of Ω_2 under excitations at 300 nm shows strong Eu^{3+}-O^{2-} covalence and high asymmetry around the Eu ion which is also consistent

with the larger values of asymmetry ratios obtained from the ratio of integrated intensities ($^5D_0 \rightarrow {}^7F_2/^5D_0 \rightarrow {}^7F_4$). The values of intensity parameters and asymmetry ratio for SNEZ-7 excited at 231 nm are significantly smaller than those of 300/395 nm excitations indicating a more symmetrical crystal environment for the Eu^{3+} ions and confirming the existence of two Eu^{3+} sites at different environments in the host lattice [50]. Besides, these results are in agreement with the XRD and Raman results wherein it was shown that there exist two sites occupied by the Eu^{3+} ions in the crystal structure. The dopant ions in these sites have different excitation energies and degree of asymmetry. Again, this result is consistent with the report in Ref. [59] which indicated that the 231 nm wavelength source excites mostly Eu^{3+} ions situated at the more symmetrical sites. The asymmetric ratios (which are similar) for the 300/395 nm excitation wavelengths is for Eu^{3+} ions situated at the lower symmetry of Zr^{4+} environment.

No band related to the $^5D_0 \rightarrow {}^7F_6$ transition was recorded in any of the emission spectra obtained in this work, hence the value of Ω_6 could not be evaluated. The computed values of radiative transition rates, A_{rad} and the corresponding radiative lifetimes (τ_{rad}) values for the SNEZ-7 sample are also presented in Table 4. Radiative lifetimes monotonically decreased with increased excitation wavelength due to reduction of non-radiative transition probabilities. Nonradiative decay rates (A_{nr}), evaluated from the relation, $1/\tau_{exp} = A_{rad} + A_{nr}$ gave values of 773, 268 and 165 s^{-1} for SNZE-7 phosphors under 230, 300 and 395 nm excitations, respectively. The A_{nr} values for 300 and 395 nm excitations are significantly smaller than the A_{nr} for the 231 nm excitation implying that the depopulation of the $^5D_0$ excited state producing the red light in SNZE-7 phosphors under these excitation wavelengths is dominated by the radiative transition probabilities. However, the non-radiative rate is higher for the indirect excitation at 231 nm confirming the existence of a different Eu^{3+} site with different radiation pathways.

The internal quantum efficiency (η) which is defined as the probability of emission of a photon per absorbed photon was obtained from the relation; $\eta = \tau_{exp}/\tau_{rad}$, where τ_{exp} is the decay lifetime value found by fitting the experimental decay profile for SNEZ-7 sample (Fig. 7). The computed values of η is highest under the CTB excitation at 300 nm (96 %) followed by direct excitation at 395 nm (41 %) where the distortions around the Eu^{3+} ions are more. The > 95% internal quantum efficiency values for SNZE-7 nanophosphors excited at 300 nm is excellent for highly efficient red light emitting phosphors with potential application in LEDs and lasers.

The obtained radiative rates calculated at different excitation wavelengths were employed in determining the laser properties of SNEZ-7 nanophosphors. One important laser property that determines whether an emission transition has the potential of lasing is the branching ratio, β. Emission transition with β > 50% is said to be a potential laser emission transition [78]. The theoretical (β$_{rad}$) and experimental (β$_{exp}$) branching ratios can be determined for a phosphor using Equations (17)–(19);

$$\beta_{rad} = \frac{A_{0-J}}{\sum A_{0-J}} \tag{14}$$

$$\beta_{exp} \frac{\int I_{0-J}(\bar{v}) d\bar{v}}{\int I_{0-1}(\bar{v}) d\bar{v}} \tag{15}$$

where all terms are as explained for Equations (7) and (8). The obtained values of experimental and calculated branching ratios are comparable as shown in Table 4. Besides, all values are greater than 50 % indicating that the $^5D_0 \rightarrow {}^7F_2$ transition of SNEZ-7 nanophosphors has the potential for lasing and better under 300 nm excitation wavelength. The simulated emission cross-section gives a better insight in the determination of potential laser performance and is expressed as;

$$\delta_e(\lambda_p) = \left[\frac{\lambda_p^4}{8\pi c n^2 \Delta \lambda_{eff}} \right] A_R \tag{16}$$

Table 5

Peak wavelength (λ_p), effective band-width ($\Delta\lambda_{eff}$), branching ratio (β) and emission cross section (δ_e) of transition levels of SNEZ-7 nanophosphors at different excitation wavelengths.

Excitation wavelength (nm)	λ_p (nm)	$\Delta\lambda_{eff}$ (nm)	β_{rad} (%)	βexp (%)	δ_e (10^{-21} cm^2)	δ_e x $\Delta\lambda_{eff}$ (10^{-28} cm^3)
231	614	55.8	57	59	2.03	11.3
300	614	61.3	63	63	3.62	22.2
395	614	55.4	58	58	4.21	23.3

where λ_p, c and $\Delta\lambda_{eff}$ are the emission peak wavelength, velocity of light and effective bandwidth given by $\Delta\lambda_{eff} = \int I(\lambda)/I_{max}d\lambda$.

The calculated values of the emission cross-sections (δ_e) at the selected excitation wavelengths (230, 300 and 395 nm) are presented in Table 5. The δ_e values are larger or comparable to those reported in literature for Eu^{3+} doped Li$_6$Y(BO$_3$)$_3$ (2.28 × 10^{-22} cm^2) [79], ZnF$_2$–PbO–TeO$_2$ (2.28 × 10^{-20} cm^2) [80], K$_2$O–SrO–Al$_2$O$_3$–P$_2$O$_5$ glasses (3.30 × 10^{-22} cm^2) [81], Eu^{3+}-doped ZnO (4.85 × 10^{-21} cm^2) [82], Tm^{3+}-doped Ba$_3$Gd$_2$(BO$_3$)$_4$ (4.85 × 10^{-21} cm^2) [83], Dy^{3+}/Gd^{3+}: SrF$_2$ (0.90 × 10^{-21} cm^2) [84,85], Yb^{3+}:Sr$_3$La$_2$(BO$_3$)$_4$ (3.07 × 10^{-21} cm^2) [85], BaLiF$_3$: Ni^{2+} (3.0 × 10^{-21} cm^2) [86], TmAl$_3$(BO$_3$)$_4$ (2.85 × 10^{-21} cm^2) [87]. The largest δ_e was found under direct excitation at 395 nm, suggesting that at this excitation wavelength, the transition uses the lowest threshold energy for the laser generation and release the highest laser gain compared to the other wavelengths. The gain bandwidth (δ_e x $\Delta\lambda_{eff}$) increased with increase of excitation wavelength, which indicates that the synthesized SNEZ-7 nanophosphors is a promising material for fibre amplifiers at 300/395 nm excitation wavelengths. The SNEZ-7 nanophosphor is a good candidate for red laser emission at 614 nm, producing comparable as well as better laser properties at 300 and 395 nm excitation wavelengths.

To assess colour purity, the CIE 1931 chromaticity coordinates of the phosphors were computed based on their PL spectra under excitation by a light source emitting at 231, 300 and 395 nm wavelengths, as depicted in Fig. 8. The corresponding CIE chromaticity coordinates for SNEZ-7 nanophosphor are detailed in Table 6. Fig. 8 illustrates that excitation of SNEZ-7 nanophosphor at all three wavelengths produced red emission is observed, with a further transition to a deep red color at 300 nm excitation wavelength. The fluorescence images in Fig. 8 underscore that SNEZ-7 nanophosphor represents a promising red phosphor for red light applications.

Correlated color temperature (CCT) was determined from the CIE 1931 XY coordinates using Equation (17) (McCamy's approximation), and the results are presented in Table 4:

$$CCT = 437n^3 + 360n^2 + 6861n + 5517 \qquad (17)$$

where $n = \frac{(x-0.3320)}{(0.1858-y)}$.

The CIE coordinates obtained for the SNEZ-7 nanophosphor are found to be similar to the National Television Standard Committee (NTSC) standards for red phosphors (0.670, 0.330), as well as the co-ordinates for various commercial red phosphors, including Y$_2$O$_2$S:Eu^{3+} (0.624, 0.337), Y$_2$O$_3$S:Eu^{3+} (0.655, 0.345), Ca$_{10}$Li(PO$_4$)$_7$:$_{0.10}$Eu^{3+} (0.638, 0.361), and Ca$_9$Y(PO$_4$)$_7$:$_{0.13}$Eu^{3+} (0.650, 0.349), commonly used in display applications [88,89]. The CIE color coordinates of all samples doped with europium are situated within the orange-red region of the chromaticity diagram, indicating low correlated color temperatures (CCTs) ranging from 2100 to 2700 K, consistent with the warmer hues typical of soft white light. Assessing phosphor performance is paramount, particularly with regards to color purity, and the CIE chromaticity diagram serves as a valuable means of precisely evaluating the color purity of the examined samples. The quantification of this color purity is expressed through equation:

$$\text{Color purity} = \frac{\sqrt{(x_i - x_s)^2 + (y_i - y_s)^2}}{\sqrt{(x_d - x_s)^2 + (y_d - y_s)^2}} \, x \, 100\% \qquad (18)$$

where (x_s, y_s) and (x_i, y_i) are the color coordinates of the light source (0.310, 0.316) and the CIE equal-energy illuminant respectively; (x_d, y_d) is the chromaticity coordinate corresponding to the dominant wavelength of light source which is (0.677, 0.322). The determined color purity falls within the range of 92.66 % and 95.07 % for 231, 300, and 395 nm, respectively indicating that the prepared phosphor emits red light with good color purity. The combination of high color purity and improved CIE chromaticity coordinates positions makes SNEZ

Table 6

CIE chromaticity coordinate and CCT of SNEZ-7 phosphors.

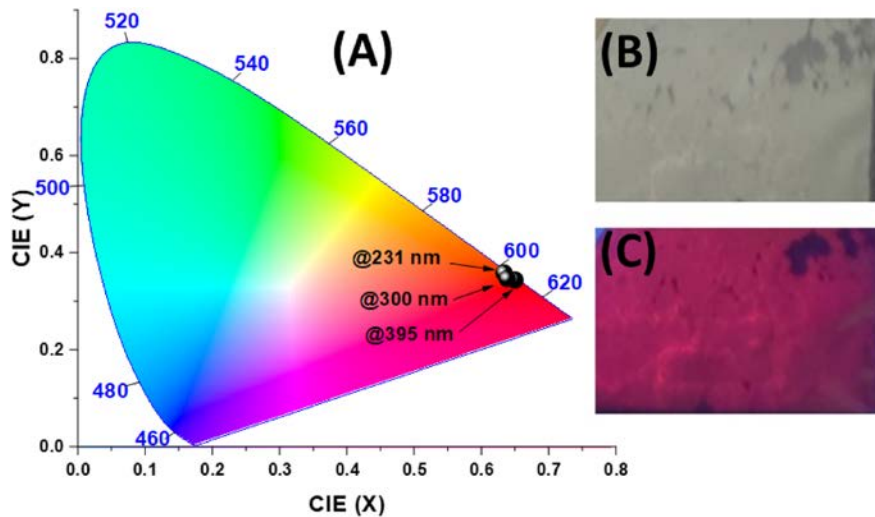| Excitation Wavelength (nm).	CIE (x)	CIE (y)	CCT (K)	Color purity (%)
231	0.634	0.357	2214	95.07
300	0.653	0.343	2797	94.23
395	0.639	0.346	2523	92.66

Fig. 8. (A) CIE chromaticity diagram for 231, 300, 395 nm excitation, (B) phosphors under natural light, (C) phosphors under 254 nm UV light of SNEZ nanophosphor.

phosphors a promising candidate for red-emitting light and a complementary light for warm white LEDs in general illumination.

4. Conclusion

Eu^{3+}-doped $Sr_{0.9-y}Na_{0.2}ZrO_3$ powders were synthesized by sol-gel method. The structure, optical and luminescent properties were studied. The samples were analyzed to determine their phase and luminescence properties using several techniques including X-ray diffraction (XRD), Raman spectroscopy, scanning electron microscopy (SEM), diffuse reflectance spectroscopy, and photoluminescence (PL) spectra. When excited at 300 nm, the SNEZ phosphor emits intense red light at 614 nm, arising from the $^5D_0 \rightarrow ^7F_2$ transition of the Eu^{3+} ions, which exhibits high sensitivity to temperature. The fluorescence image of the phosphor under UV lamp show that SNZE-7 nanophosphors excited with 300 nm wavelength source is capable of emitting red light with high internal quantum efficiency of 96 %, high colour purity, and a comparable CIE coordinates with standard and commercial red light emitting phosphors By conducting precise computations of Judd-Ofelt intensity parameters (Ω_2, Ω_4), radiative parameters (A_{rad}), experimental lifetime (τ_{rad}), quantum efficiency (η), asymmetry ratios (R_0), effective bandwidth ($\Delta\lambda_{eff}$), branching ratio (β), and emission cross section (δe), it is apparent that SNEZ nanophosphors are exceptionally well-suited to serve as an efficient laser systems relying on the photoluminescence phenomenon.

CRediT authorship contribution statement

A. Nathan-Abutu: Writing – original draft, Methodology, Investigation, Data curation. **I. Ahemen:** Writing – review & editing, Formal analysis, Data curation, Conceptualization. **R.E. Kroon:** Writing – review & editing, Investigation, Formal analysis. **A. Reyes-Rojas:** Writing – review & editing, Validation, Supervision, Project administration, Methodology, Investigation, Formal analysis, Data curation, Conceptualization.

Declaration of competing interest

The authors declare that they do not have any identifiable conflicting financial interests or personal connections that might have seemed to impact the research presented in this article.

Acknowledgement

Data availability

Data will be made available on request.

References

[1] M.A. Peña, J.L.G. Fierro, Chemical structures and performance of perovskite oxides, Chem. Rev. 101 (7) (2001) 1981–2018.

[2] A. Ahtee, M. Ahtee, A.M. Glazer, A.W. Hewat, The structure of orthorhombic SrZrO3 by neutron powder diffraction, Acta Crystallogr. B 32 (12) (1976) 3243–3246.

[3] J.A.M. van Roosmalen, P. van Vlaanderen, E.H.P. Cordfunke, On the structure of SrZrO3, J. Solid State Chem. 101 (1) (1992) 59–65.

[4] R. Cao, H. Liang, T. Chen, Z. Wu, Z. Jiang, X. Yi, J. Wen, Q. Zhong, Study on luminescence characterizations of SrMg2La2W2O12:Eu3+ red-emitting phosphor, J. Phys. Chem. Solid. 163 (2022) 110569.

[5] N. Vazquez-Flores, C.J. Salas-Juárez, R.I. López-Esquivel, D. Nolasco-Altamirano, M.A. Ugalde-Valdés, J.C. Guzmán-Olguín, R. García-Salcedo, J. Guzmán-Mendoza, J.C. Earthman, T. Rivera-Montalvo, Thermally stimulated luminescence of BaZrO3: Eu3+ nanopowders for dosimetric applications, Opt. Mater. 147 (2024) 114740.

[6] G. Annadurai, S.M.M. Kennedy, Synthesis and photoluminescence properties of Ba2CaZn2Si6O17:Eu3+ red phosphors for white LED applications, J. Lumin. 169 (2016) 690–694.

[7] B. Evangeline, P.A. Azeem, R. Prasada Rao, G. Swati, D. Haranath, Structural and luminescent features of cerium doped CaZrO3 blue nanophosphors, J. Alloys Compd. 705 (2017) 618–623.

[8] A. Nathan, J. Rex, A. Roy, Luminescence characteristics of polymer passivized strontium aluminate phosphor, Physical Science International Journal 8 (3) (2015) 1–6.

[9] J. Park, L. Gao, Advancements in fluorescence lifetime imaging microscopy Instrumentation: towards high speed and 3D, Curr. Opin. Solid State Mater. Sci. 30 (2024) 101147.

[10] S. Yuan, Z. Mu, L. Lou, S. Zhao, D. Zhu, F. Wu, Broadband NIR-II phosphors with Cr4+ single activated centers based on special crystal structure for nondestructive analysis, Ceram. Int. 48 (18) (2022) 26884–26893.

[11] M. Liao, Q. Wang, Q. Lin, M. Xiong, X. Zhang, H. Dong, Z. Lin, M. Wen, D. Zhu, Z. Mu, F. Wu, Na replaces Rb towards high-performance narrow-band green phosphors for backlight display applications, Adv. Opt. Mater. 9 (17) (2021).

[12] S. Guo, S. Zhang, Z. Mu, F. Wu, X. Feng, Q. Zhang, J. Feng, D. Zhu, Q. Du, Enhanced near infrared luminescence of Lu2GeO5: Nd3+ by the co-doping of Bi3+, J. Lumin. 206 (2019) 278–283.

[13] S.K. Gupta, N. Pathak, R.M. Kadam, An efficient gel-combustion synthesis of visible light emitting barium zirconate perovskite nanoceramics: probing the photoluminescence of Sm3+ and Eu3+ doped BaZrO3, J. Lumin. 169 (2016) 106–114.

[14] P. Psuja, D. Hreniak, W. Strek, Rare-earth doped nanocrystalline phosphors for field emission displays, J. Nanomater. 1–7 (2007) (2007).

[15] A.K. Kunti, N. Patra, R.A. Harris, S.K. Sharma, D. Bhattacharyya, S.N. Jha, H. C. Swart, Structural properties and luminescence dynamics of CaZrO3:Eu3+ phosphors, Inorg. Chem. Front. 8 (3) (2021) 821–836.

[16] P. Dang, D. Liu, Y. Wei, G. Li, H. Lian, M. Shang, J. Lin, Highly efficient cyan-green emission in self-activated Rb3RV2O8 (R = Y, Lu) vanadate phosphors for full-spectrum white light-emitting diodes (LEDs), Inorg. Chem. 59 (9) (2020) 6026–6038.

[17] A.K. Kunti, N. Patra, R.A. Harris, S.K. Sharma, D. Bhattacharyya, S.N. Jha, H. C. Swart, Local structure and spectroscopic properties of Eu3+ -doped BaZrO3, Inorg. Chem. 58 (5) (2019) 3073–3089.

[18] S. Shisina, S. Das, S. Som, S. Ahmad, V. Vinduja, P. Merin, K.G. Nishanth, P. Kumari, M.K. Pandey, Structure and optoelectronic properties of palmierite structured Ba2Y0.67δ0.33V2O8: Eu3+ red phosphors for n-UV and blue diode based warm white light systems, J. Alloys Compd. 802 (2019) 723–732.

[19] S. Nakamura, G. Fasol, The Blue Laser Diode: GaN Based Light Emitters and Lasers, Springer Science & Business Media, 2013.

[20] D. Valiev, T. Han, V. Vaganov, S. Stepanov, The effect of Ce3+ concentration and heat treatment on the luminescence efficiency of YAG phosphor, J. Phys. Chem. Solid. 116 (2018) 1–6.

[21] M. Guzik, E. Tomaszewicz, Y. Guyot, J. Legendziewicz, G. Boulon, Eu3+ luminescence from different sites in a scheelite-type cadmium molybdate red phosphor with vacancies, J Mater Chem C Mater 3 (33) (2015) 8582–8594.

[22] J.-C. Zhang, Y.-Z. Long, H.-D. Zhang, B. Sun, W.-P. Han, X.-Y. Sun, Eu2+/Eu3+ -emission-ratio-tunable CaZr(PO4)2 :Eu phosphors synthesized in air atmosphere for potential white light-emitting deep UV LEDs, J. Mater. Chem. C 2 (2) (2014) 312–318.

[23] W. Ran, L. Wang, W. Zhang, F. Li, H. Jiang, W. Li, L. Su, R. Houzong, X. Pan, J. Shi, A super energy transfer process based S-shaped cluster in ZnMoO4 phosphors: theoretical and experimental investigation, J Mater Chem C Mater 3 (32) (2015) 8344–8350.

[24] H. Ji, Z. Huang, Z. Xia, M.S. Molokeev, V.v. Atuchin, M. Fang, S. Huang, New yellow-emitting whitlockite-type structure Sr1.75Ca1.25(PO4)2:Eu2+ phosphor for near-UV pumped white light-emitting devices, Inorg. Chem. 53 (10) (2014) 5129–5135.

[25] S. Katyayan, S. Agrawal, Investigation of spectral properties of Eu3+ and Tb3+ doped strontium zirconium trioxide orthorhombic perovskite for optical and sensing applications, J. Mater. Sci. Mater. Electron. 28 (24) (2017) 18442–18454.

[26] P. Ctibor, After-glow luminescence of SrZrO3 prepared by plasma spraying, Bol. Soc. Espanola Ceram. Vidr. 57 (5) (2018) 190–194.

[27] Sheetal, V.B. Taxak, R. Arora, Dayawati, S.P. Khatkar, Synthesis, structural and optical properties of SrZrO3:Eu3+ phosphor, J. Rare Earths 32 (4) (2014) 293–297.

[28] S. Katyayan, S. Agrawal, Study of optical behaviour of Eu3+ and Tb3+ doped zirconate perovskite phosphors prepared by molten salt technique, Opt. Quant. Electron. 52 (1) (2020) 18.

[29] N. Singh, M. Seshadri, M.S. Pathak, V. Singh, Structural and photoluminescence properties of orange emitting perovskites SrZrO3:Sm3+ phosphors for solid-state lighting, Solid State Sci. 87 (2019) 163–170.

[30] M. Venugopal, H.P. Kumar, R. Jayakrishnan, Synthesis, characterization and photoluminescent properties of Sm3+/Dy3+ doped strontium zirconate perovskites, J. Electroceram. 44 (3–4) (2020) 163–172.

[31] T.J. Pérez-Juache, R. López-Juárez, E. Barrera-Calva, F. González, Luminescent properties of Pr3+-doped SrZrO3 phosphors, J. Lumin. 192 (2017) 599–607.

[32] N. Singh, I.-W. Kim, S. Watanabe, T.K. Gundu Rao, V. Singh, Trivalent gadolinium doped SrZrO₃ perovskite ceramic: sol-gel synthesis, paramagnetic centres, and luminescence studies, Ceram. Int. 46 (14) (2020) 22108–22115.

[33] K. Binnemans, Interpretation of europium (III) spectra, Coord. Chem. Rev. 295 (2015) 1–45.

[34] J.-C.G. Bünzli, Review: lanthanide coordination chemistry: from old concepts to coordination polymers, J. Coord. Chem. 67 (23–24) (2014) 3706–3733.

[35] A. Nathan-Abutu, I. Ahemen, A. Reyes-Rojas, Structural and optical investigation of novel Sr₁₋ₓNaₓZrO₃ perovskite nanoparticles, Physica B Condens Matter 653 (2023) 414655.

[36] R.D. Shannon, Revised effective ionic radii and systematic studies of interatomic distances in halides and chalcogenides, Acta Crystallogr. A 32 (5) (1976) 751–767.

[37] Y.Q. Jia, Crystal radii and effective ionic radii of the rare earth ions, J. Solid State Chem. 95 (1) (1991) 184–187.

[38] A.K. Parchur, R.S. Ningthoujam, Behaviour of electric and magnetic dipole transitions of Eu³⁺, ⁵D₀ → ⁷F₀ and Eu–O charge transfer band in Li⁺ co-doped YPO₄:Eu³⁺, RSC Adv. 2 (29) (2012) 10859.

[39] I. Ahemen, F.B. Dejene, R.E. Kroon, H.C. Swart, Effect of europium ion concentration on the structural and photoluminescence properties of novel Li₂BaZrO₄:Eu³⁺ nanocrystals, Opt. Mater. 74 (2017) 58–66.

[40] O. Kalu, A.N. Abutu, H. Esparza Ponce, A. Ramirez-DelaCruz, R.E. Kroon, A. Reyes-Rojas, Structural and optical characterization of RF sputtered CdMgZnO thin film with different Cd concentrations, Mater. Chem. Phys. 308 (2023) 128314.

[41] J. Lu, Z. Mu, D. Zhu, Q. Wang, F. Wu, Luminescence properties of Eu³⁺ doped La₃Ga₅GeO₁₄ and effect of Bi³⁺ co-doping, J. Lumin. 196 (2018) 50–56.

[42] Z. Liang, Z. Mu, Q. Wang, D. Zhu, F. Wu, The synthesis and luminescence properties of a novel red-emitting phosphor: Eu³⁺-doped Ca₉La(PO₄)₇, Appl. Phys. A 123 (10) (2017) 612.

[43] P.R. Jubu, O.S. Obaseki, A. Nathan-Abutu, F.K. Yam, Y. Yusof, M.B. Ochang, Dispensability of the conventional Tauc's plot for accurate bandgap determination from UV–vis optical diffuse reflectance data, Results in Optics 9 (2022) 100273.

[44] K.C. Sushma, S. Kumar, G. Nagaraju, D.P. Aarti, M.B.M. Reddy, M.S. Rudresha, R. B. Basavaraj, Color tunable SrZrO₃:Sm³⁺ nanopowders with satisfactory photoluminescent, band engineering properties for warm white LEDs and advanced forensic applications, J. Mol. Struct. 1254 (2022) 132302.

[45] Z. Guo, B. Sa, B. Pathak, J. Zhou, R. Ahuja, Z. Sun, Band gap engineering in huge-gap semiconductor SrZrO₃ for visible-light photocatalysis, Int. J. Hydrogen Energy 39 (5) (2014) 2042–2048.

[46] L.S. Cavalcante, A.Z. Simões, J.C. Sczancoski, V.M. Longo, R. Erlo, M.T. Escote, E. Longo, J.A. Varela, SrZrO₃ powders obtained by chemical method: synthesis, characterization and optical absorption behaviour, Solid State Sci. 9 (11) (2007) 1020–1027.

[47] Y.S. Malghe, U.C. Yadav, Synthesis, characterization and investigation of dielectric properties of nanosized SrZrO₃, J. Therm. Anal. Calorim. 122 (2) (2015) 589–594.

[48] M. Shivaram, H. Nagabhushana, S.C. Sharma, S.C. Prashantha, B. Daruka Prasad, N. Dhananjaya, R. Hari Krishna, B.M. Nagabhushana, C. Shivakumara, R.P. S. Chakradhar, Synthesis and luminescence properties of Sm³⁺ doped CaTiO₃ nanophosphor for application in white LED under NUV excitation, Spectrochim. Acta Mol. Biomol. Spectrosc. 128 (2014) 891–901.

[49] A. Slodczyk, P. Colomban, S. Upasen, F. Grasset, G. André, Structural stability of anhydrous proton conducting SrZr₀.₉Er₀.₁O₃₋δ perovskite ceramic vs. protonation/ deprotonation cycling: neutron diffraction and Raman studies, J. Phys. Chem. Solid. 83 (2015) 85–95.

[50] T. Hahn, U. Shmueli, J.W. Arthur, International Tables for Crystallography, 1, 1983, p. 198, 182.

[51] S.N. Shkerin, A.V. Rudakova, K.M. Bulanin, A.S. Khaliullina, A.N. Meshcherskikh, E.G. Vovkotrub, L.A. Dunyushkina, Raman spectroscopy of SrZrO₃ based proton conducting electrolyte: effect of Y-doping and Sr-nonstoichiometry, Int. J. Hydrogen Energy 46 (32) (2021) 17007–17018.

[52] A. Nathan-Abutu, I. Ahemen, R.E. Kroon, A. Reyes-Rojas, Downshifting photoluminescence of Erbium doped NaSrZrO₃ for solid-state lighting, J. Alloys Compd. 987 (2024) 174104.

[53] K. Sedeek, N. Makram, H. Hantour, T.Z. Amer, S.A. Said, An explicit and novel structure, lattice dynamics, and photoemission of La-doped nanocrystalline SrZrO₃ perovskite, Rare Met. 40 (1) (2021) 105–112.

[54] M. Tarrida, H. Larguem, M. Madon, Structural investigations of (Ca,Sr)ZrO₃ and Ca (Sn,Zr)O₃ perovskite compounds, Phys. Chem. Miner. 36 (7) (2009) 403–413.

[55] A. Slodczyk, M.-H. Limage, P. Colomban, O. Zaafrani, F. Grasset, J. Loricourt, B. Sala, Substitution and proton doping effect on SrZrO₃ behaviour: high-pressure Raman study, J. Raman Spectrosc. 42 (12) (2011) 2089–2099.

[56] A. Mineshige, Oxygen nonstoichiometry in SrCeO₃-based high-temperature protonic conductors evaluated by Raman spectroscopy, Solid State Ionics 162–163 (2003) 41–45.

[57] S. Das, C.-Y. Yang, C.-H. Lu, Structural and optical properties of tunable warm-white light-emitting ZrO₂ :Dy³⁺-Eu³⁺ nanocrystals, J. Am. Ceram. Soc. 96 (5) (2013) 1602–1609.

[58] I. Ahemen, F.B. Dejene, R. Botha, Strong green-light emitting Tb³⁺ doped tetragonal ZrO₂ nanophosphors stabilized by Ba²⁺ ions, J. Lumin. 201 (2018) 303–313.

[59] I. Ahemen, F.B. Dejene, Site spectroscopy probing of Eu³⁺ incorporated into novel LiYSrZrO₃₊α host matrix, Curr. Appl. Phys. 18 (11) (2018) 1359–1367.

[60] B.F. dos Santos, R.M. Araujo, M.E.G. Valerio, M.V. dos S. Rezende, Optical spectroscopy study of YVO₄:Eu³⁺ nanopowders prepared by the proteic sol–gel route, Solid State Sci. 42 (2015) 45–51.

[61] I. Ahemen, O. Meludu, F.B. Dejene, B. Viana, Site spectroscopy of Eu³⁺ doped- ZnS nanocrystals embedded in sodium carboxymethyl cellulose matrix, Opt. Mater. 61 (2016) 82–91.

[62] Q. Li, S. Zhang, W. Lin, W. Li, Y. Li, Z. Mu, F. Wu, A warm white emission of Bi³⁺-Eu³⁺ and Bi³⁺-Sm³⁺ codoping Lu₂Ge₂O₇ phosphors by energy transfer of Bi³⁺-sensitized Eu³⁺/Sm³⁺, Spectrochim. Acta Mol. Biomol. Spectrosc. 228 (2020) 117755.

[63] M. Liao, Z. Mu, S. Zhang, F. Wu, Z. Nie, Z. Zheng, X. Feng, Q. Zhang, J. Feng, D. Zhu, A red phosphor Mg₃Y₂Ge₃O₁₂: Bi³⁺, Eu³⁺ with high brightness and excellent thermal stability of luminescence for white light-emitting diodes, J. Lumin. 210 (2019) 202–209.

[64] W. Li, M. Qiu, Y. Li, S. Zhang, Q. Li, W. Lin, Z. Mu, F. Wu, Energy transfer and multicolor-tunable emissions of Sr₃La₆(SiO₄)₆:Ce³⁺, Tb³⁺, Eu³⁺, J. Electron. Mater. 49 (2) (2020) 1404–1411.

[65] P.A. Tanner, Some misconceptions concerning the electronic spectra of tri-positive europium and cerium, Chem. Soc. Rev. 42 (12) (2013) 5090.

[66] S.K. Gupta, H. Abdou, C.U. Segre, Y. Mao, Excitation-dependent photoluminescence of BaZrO₃:Eu³⁺ crystals, Nanomaterials 12 (17) (2022) 3028.

[67] X.Y. Chen, G.K. Liu, The standard and anomalous crystal-field spectra of Eu³⁺, J. Solid State Chem. 178 (2) (2005) 419–428.

[68] Q. Ju, Y. Liu, R. Li, L. Liu, W. Luo, X. Chen, Optical spectroscopy of Eu³⁺ -doped BaFCl nanocrystals, J. Phys. Chem. C 113 (6) (2009) 2309–2315.

[69] S.K. Gupta, P.S. Ghosh, N. Pathak, A. Arya, V. Natarajan, Understanding the local environment of Sm³⁺ in doped SrZrO₃ and energy transfer mechanism using time-resolved luminescence: a combined theoretical and experimental approach, RSC Adv. 4 (55) (2014) 29202–29215.

[70] K. Thomas, D. Alexander, K.P. Mani, S. Gopi, S. Ajeesh Kumar, P.R. Biju, N. V. Unnikrishnan, C. Joseph, Intrinsic red luminescence of Eu³⁺-activated lanthanum molybdate: insights into the spectroscopic features using Judd–Ofelt theoretical analysis, J. Phys. Chem. Solid. 137 (2020) 109212.

[71] A. Ćirić, S. Stojadinović, M. Sekulić, M.D. Dramićanin, JOES: an application software for Judd-Ofelt analysis from Eu³⁺ emission spectra, J. Lumin. 205 (2019) 351–356.

[72] W.T. Carnall, P.R. Fields, K. Rajnak, Electronic energy levels in the trivalent lanthanide aquo ions. I. Pr³⁺, Nd³⁺, Pm³⁺, Sm³⁺, Dy³⁺, Ho³⁺, Er³⁺, and Tm³⁺, J. Chem. Phys. 49 (10) (1968) 4424–4442.

[73] C. Mbakaan, I. Ahemen, A.D. Onojah, A.N. Amah, K.G. Tshabalala, F.B. Dejene, Luminescent properties of Eu³⁺-doped silica nanophosphors derived from rice husk, Opt. Mater. 108 (2020) 110168.

[74] C. Görller-Walrand, K. Binnemans, Chapter 167 Spectral Intensities of F-F Transitions, 1998, pp. 101–264.

[75] A. Ćirić, S. Stojadinović, M.D. Dramićanin, An extension of the Judd-Ofelt theory to the field of lanthanide thermometry, J. Lumin. 216 (2019) 116749.

[76] V. Dimitrov, S. Sakka, Linear and nonlinear optical properties of simple oxides. II, J. Appl. Phys. 79 (3) (1996) 1741–1745.

[77] K.C. Sushma, R.B. Basavaraj, D.P. Aarti, M.B.M. Reddy, G. Nagaraju, M. S. Rudresha, H.M.S. Kumar, K.N. Venkatachalaiah, Efficient red-emitting SrZrO₃: Eu³⁺ phosphor superstructures for display device applications, J. Mol. Struct. 1283 (2023) 135192.

[78] M.P. Hehlen, M.G. Brik, K.W. Krämer, 50th anniversary of the Judd–Ofelt theory: an experimentalist's view of the formalism and its application, J. Lumin. 136 (2013) 221–239.

[79] E. Kaewnuam, N. Chanthima, C.K. Jayasankar, H.J. Kim, J. Kaewkhao, Optical, luminescence and judd-oflet study of Eu³⁺ doped lithium yttrium borate glasses for using as laser gain medium, Key Eng. Mater. 675–676 (2016) 364–367.

[80] V. Ravi Kumar, N. Veeraiah, S. Appa Rao, S. Bhuddudu, Optical absorption and photoluminescence properties of Eu³⁺-doped ZnF₂–PbO–TeO₂ glasses, J. Mater. Sci. 33 (10) (1998) 2659–2662.

[81] K.U. Kumar, S.S. Babu, Ch S. Rao, C.K. Jayasankar, Optical and fluorescence spectroscopy of Eu₂O₃-doped P₂O₅–K₂O–KF–MO–Al₂O₃ (M = Mg, Sr and Ba) glasses, Opt Commun. 284 (12) (2011) 2909–2914.

[82] S. Bebars, A.-S. Gadallah, M.A. Khedr, M.T.H. Abou Kana, Judd-Ofelt and laser parameters of Eu³⁺ ions doped in network restricted matrices, J. Lumin. 192 (2017) 949–956.

[83] Y. Wei, C. Tu, G. Jia, Z. You, H. Wang, F. Yang, X. Lu, J. Li, Z. Zhu, Y. Wang, Spectroscopic properties of Tm³⁺ -doped Ba₃Gd₂(BO₃)₄ crystal, Solid State Commun. 140 (5) (2006) 230–235.

[84] H. Wang, X. Gao, Y. Wang, Z. Zhu, Z. You, J. Li, G. Lakshminarayana, C. Tu, Optimizing yellow fluorescence in Dy³⁺:SrF₂ crystal through Gd³⁺ co-doping, J. Mater. Sci. Mater. Electron. 34 (10) (2023) 927.

[85] J. Pan, Z. Lin, Z. Hu, L. Zhang, G. Wang, Crystal growth and spectral properties of Yb³⁺:Sr₃La₂(BO₃)₄ crystal, Opt. Mater. 28 (3) (2006) 250–254.

[86] E. Martins, N.D. Vieira, S.L. Baldochi, S.P. Morato, J.Y. Gesland, Optical spectroscopy of BaLiF₃ doped with Ni²⁺, J. Lumin. 62 (6) (1994) 281–289.

[87] G. Jia, C. Tu, J. Li, Z. You, Z. Zhu, B. Wu, Crystal structure, Judd−Ofelt analysis, and spectroscopic assessment of a TmAl₃(BO₃)₄ crystal as a new potential diode-pumped laser near 1.9 µm, Inorg. Chem. 45 (23) (2006) 9326–9331.

[88] G. Dong, G. Ma, Y. Liu, Z. Yang, Q. Liu, Synthesis and photoluminescence properties of the high-brightness Eu³⁺-doped Sr₃Bi(PO₄)₃ phosphors, Opt Commun. 285 (20) (2012) 4097–4101.

[89] B. Wang, Y. Lin, H. Ju, Luminescence properties of red-emitting Ca₉Y(PO₄)₇: Eu³⁺ phosphor for NUV white-LEDs, J. Alloys Compd. 584 (2014) 167–170.